

1
2
3
4
5
6
7
8
9
10
11
12
13
14
15
16
17
18
19
20
21
22
23
24
25
26
27
28
29
30
31

Observation of Supernova Remnant IC 443 with the Fermi Large Area Telescope

A. A. Abdo^{1,2}, M. Ackermann³, M. Ajello³, L. Baldini⁴, J. Ballet⁵, G. Barbiellini^{6,7},
D. Bastieri^{8,9}, B. M. Baughman¹⁰, K. Bechtol³, R. Bellazzini⁴, B. Berenji³, R. D. Blandford³,
E. D. Bloom³, E. Bonamente^{11,12}, A. W. Borgland³, J. Bregeon⁴, A. Brez⁴, M. Brigida^{13,14},
P. Bruel¹⁵, T. H. Burnett¹⁶, S. Buson⁹, G. A. Caliandro^{13,14}, R. A. Cameron³, P. A. Caraveo¹⁷,
J. M. Casandjian⁵, C. Cecchi^{11,12}, Ö. Çelik^{18,19,20}, A. Chekhtman^{1,21}, C. C. Cheung¹⁸, J. Chiang³,
A. N. Cillis¹⁸, S. Ciprini^{11,12}, R. Claus³, J. Cohen-Tanugi²², L. R. Cominsky²³, J. Conrad^{24,25,26},
S. Cutini²⁷, C. D. Dermer¹, A. de Angelis²⁸, F. de Palma^{13,14}, E. do Couto e Silva³, P. S. Drell³,
A. Drlica-Wagner³, R. Dubois³, D. Dumora^{29,30}, C. Farnier²², C. Favuzzi^{13,14}, S. J. Fegan¹⁵,
W. B. Focke³, P. Fortin¹⁵, M. Frailis²⁸, Y. Fukazawa³¹, S. Funk³, P. Fusco^{13,14}, F. Gargano¹⁴,
D. Gasparrini²⁷, N. Gehrels^{18,32}, S. Germani^{11,12}, G. Giavitto³³, B. Giebels¹⁵, N. Giglietto^{13,14},
F. Giordano^{13,14}, T. Glanzman³, G. Godfrey³, I. A. Grenier⁵, M.-H. Grondin^{29,30}, J. E. Grove¹,
L. Guillemot^{29,30}, S. Guiriec³⁴, Y. Hanabata³¹, A. K. Harding¹⁸, M. Hayashida³, R. E. Hughes¹⁰,
M. S. Jackson^{24,25,35}, G. Jóhannesson³, A. S. Johnson³, T. J. Johnson^{18,32}, W. N. Johnson¹,
T. Kamae³, H. Katagiri³¹, J. Kataoka^{36,37}, N. Kawai^{36,38}, M. Kerr¹⁶, J. Knödseder³⁹,
M. L. Kocian³, M. Kuss⁴, J. Lande³, L. Latronico⁴, S.-H. Lee³, M. Lemoine-Goumard^{29,30},
F. Longo^{6,7}, F. Loparco^{13,14}, B. Lott^{29,30}, M. N. Lovellette¹, P. Lubrano^{11,12}, G. M. Madejski³,
A. Makeev^{1,21}, M. N. Mazziotta¹⁴, C. Meurer^{24,25}, P. F. Michelson³, W. Mitthumsiri³,
A. A. Moiseev^{19,32}, C. Monte^{13,14}, M. E. Monzani³, A. Morselli⁴⁰, I. V. Moskalenko³, S. Murgia³,
T. Nakamori³⁶, P. L. Nolan³, J. P. Norris⁴¹, E. Nuss²², T. Ohsugi³¹, E. Orlando⁴², J. F. Ormes⁴¹,
M. Ozaki⁴³, D. Paneque³, J. H. Panetta³, D. Parent^{29,30}, V. Pelassa²², M. Pepe^{11,12},
M. Pesce-Rollins⁴, F. Piron²², T. A. Porter⁴⁴, S. Rainò^{13,14}, R. Rando^{8,9}, M. Razzano⁴,
A. Reimer^{45,3}, O. Reimer^{45,3}, T. Reposeur^{29,30}, L. S. Rochester³, A. Y. Rodriguez⁴⁶,
R. W. Romani³, M. Roth¹⁶, F. Ryde^{35,25}, H. F.-W. Sadrozinski⁴⁴, D. Sanchez¹⁵, A. Sander¹⁰,
P. M. Saz Parkinson⁴⁴, J. D. Scargle⁴⁷, C. Sgrò⁴, E. J. Siskind⁴⁸, D. A. Smith^{29,30}, P. D. Smith¹⁰,
G. Spandre⁴, P. Spinelli^{13,14}, M. S. Strickman¹, A. W. Strong⁴², D. J. Suson⁴⁹, H. Tajima³,
H. Takahashi³¹, T. Takahashi⁴³, T. Tanaka³, J. B. Thayer³, J. G. Thayer³, D. J. Thompson¹⁸,
L. Tibaldo^{8,5,9}, D. F. Torres^{50,46}, G. Tosti^{11,12}, A. Tramacere^{3,51}, Y. Uchiyama^{43,3}, T. L. Usher³,
A. Van Etten³, V. Vasileiou^{18,19,20}, C. Venter^{18,52}, N. Vilchez³⁹, V. Vitale^{40,53}, A. P. Waite³,
P. Wang³, B. L. Winer¹⁰, K. S. Wood¹, T. Ylinen^{35,54,25}, M. Ziegler⁴⁴

-
- ¹Space Science Division, Naval Research Laboratory, Washington, DC 20375, USA
- ²National Research Council Research Associate, National Academy of Sciences, Washington, DC 20001, USA
- ³W. W. Hansen Experimental Physics Laboratory, Kavli Institute for Particle Astrophysics and Cosmology, Department of Physics and SLAC National Accelerator Laboratory, Stanford University, Stanford, CA 94305, USA
- ⁴Istituto Nazionale di Fisica Nucleare, Sezione di Pisa, I-56127 Pisa, Italy
- ⁵Laboratoire AIM, CEA-IRFU/CNRS/Université Paris Diderot, Service d'Astrophysique, CEA Saclay, 91191 Gif sur Yvette, France
- ⁶Istituto Nazionale di Fisica Nucleare, Sezione di Trieste, I-34127 Trieste, Italy
- ⁷Dipartimento di Fisica, Università di Trieste, I-34127 Trieste, Italy
- ⁸Istituto Nazionale di Fisica Nucleare, Sezione di Padova, I-35131 Padova, Italy
- ⁹Dipartimento di Fisica “G. Galilei”, Università di Padova, I-35131 Padova, Italy
- ¹⁰Department of Physics, Center for Cosmology and Astro-Particle Physics, The Ohio State University, Columbus, OH 43210, USA
- ¹¹Istituto Nazionale di Fisica Nucleare, Sezione di Perugia, I-06123 Perugia, Italy
- ¹²Dipartimento di Fisica, Università degli Studi di Perugia, I-06123 Perugia, Italy
- ¹³Dipartimento di Fisica “M. Merlin” dell’Università e del Politecnico di Bari, I-70126 Bari, Italy
- ¹⁴Istituto Nazionale di Fisica Nucleare, Sezione di Bari, 70126 Bari, Italy
- ¹⁵Laboratoire Leprince-Ringuet, École polytechnique, CNRS/IN2P3, Palaiseau, France
- ¹⁶Department of Physics, University of Washington, Seattle, WA 98195-1560, USA
- ¹⁷INAF-Istituto di Astrofisica Spaziale e Fisica Cosmica, I-20133 Milano, Italy
- ¹⁸NASA Goddard Space Flight Center, Greenbelt, MD 20771, USA
- ¹⁹Center for Research and Exploration in Space Science and Technology (CRESST), NASA Goddard Space Flight Center, Greenbelt, MD 20771, USA
- ²⁰University of Maryland, Baltimore County, Baltimore, MD 21250, USA
- ²¹George Mason University, Fairfax, VA 22030, USA
- ²²Laboratoire de Physique Théorique et Astroparticules, Université Montpellier 2, CNRS/IN2P3, Montpellier, France
- ²³Department of Physics and Astronomy, Sonoma State University, Rohnert Park, CA 94928-3609, USA
- ²⁴Department of Physics, Stockholm University, AlbaNova, SE-106 91 Stockholm, Sweden
- ²⁵The Oskar Klein Centre for Cosmoparticle Physics, AlbaNova, SE-106 91 Stockholm, Sweden
- ²⁶Royal Swedish Academy of Sciences Research Fellow, funded by a grant from the K. A. Wallenberg Foundation
- ²⁷Agenzia Spaziale Italiana (ASI) Science Data Center, I-00044 Frascati (Roma), Italy
- ²⁸Dipartimento di Fisica, Università di Udine and Istituto Nazionale di Fisica Nucleare, Sezione di Trieste, Gruppo Collegato di Udine, I-33100 Udine, Italy
- ²⁹Université de Bordeaux, Centre d’Études Nucléaires Bordeaux Gradignan, UMR 5797, Gradignan, 33175, France

ABSTRACT

We report observation of the supernova remnant IC 443 (G189.1+3.0) with the *Fermi Gamma-ray Space Telescope* Large Area Telescope (LAT) in the energy band between 200 MeV and 50 GeV. IC 443 is a shell-type supernova remnant with mixed

³⁰CNRS/IN2P3, Centre d'Études Nucléaires Bordeaux Gradignan, UMR 5797, Gradignan, 33175, France

³¹Department of Physical Sciences, Hiroshima University, Higashi-Hiroshima, Hiroshima 739-8526, Japan

³²University of Maryland, College Park, MD 20742, USA

³³Istituto Nazionale di Fisica Nucleare, Sezione di Trieste, and Università di Trieste, I-34127 Trieste, Italy

³⁴University of Alabama in Huntsville, Huntsville, AL 35899, USA

³⁵Department of Physics, Royal Institute of Technology (KTH), AlbaNova, SE-106 91 Stockholm, Sweden

³⁶Department of Physics, Tokyo Institute of Technology, Meguro City, Tokyo 152-8551, Japan

³⁷Waseda University, 1-104 Totsukamachi, Shinjuku-ku, Tokyo, 169-8050, Japan

³⁸Cosmic Radiation Laboratory, Institute of Physical and Chemical Research (RIKEN), Wako, Saitama 351-0198, Japan

³⁹Centre d'Étude Spatiale des Rayonnements, CNRS/UPS, BP 44346, F-30128 Toulouse Cedex 4, France

⁴⁰Istituto Nazionale di Fisica Nucleare, Sezione di Roma "Tor Vergata", I-00133 Roma, Italy

⁴¹Department of Physics and Astronomy, University of Denver, Denver, CO 80208, USA

⁴²Max-Planck Institut für extraterrestrische Physik, 85748 Garching, Germany

⁴³Institute of Space and Astronautical Science, JAXA, 3-1-1 Yoshinodai, Sagamihara, Kanagawa 229-8510, Japan

⁴⁴Santa Cruz Institute for Particle Physics, Department of Physics and Department of Astronomy and Astrophysics, University of California at Santa Cruz, Santa Cruz, CA 95064, USA

⁴⁵Institut für Astro- und Teilchenphysik and Institut für Theoretische Physik, Leopold-Franzens-Universität Innsbruck, A-6020 Innsbruck, Austria

⁴⁶Institut de Ciències de l'Espai (IEEC-CSIC), Campus UAB, 08193 Barcelona, Spain

⁴⁷Space Sciences Division, NASA Ames Research Center, Moffett Field, CA 94035-1000, USA

⁴⁸NYCB Real-Time Computing Inc., Lattingtown, NY 11560-1025, USA

⁴⁹Department of Chemistry and Physics, Purdue University Calumet, Hammond, IN 46323-2094, USA

⁵⁰Institució Catalana de Recerca i Estudis Avançats, Barcelona, Spain

⁵¹Consorzio Interuniversitario per la Fisica Spaziale (CIFS), I-10133 Torino, Italy

⁵²North-West University, Potchefstroom Campus, Potchefstroom 2520, South Africa

⁵³Dipartimento di Fisica, Università di Roma "Tor Vergata", I-00133 Roma, Italy

⁵⁴School of Pure and Applied Natural Sciences, University of Kalmar, SE-391 82 Kalmar, Sweden

Corresponding authors: T. Kamae (kamae@slac.stanford.edu), S.-H. Lee (shia520@stanford.edu), D. F. Torres (dtorres@ieec.uab.es), A. Y. Rodriguez (arodrig@ieec.uab.es) and F. Giordano (francesco.giordano@ba.infn.it)

morphology located off the outer Galactic plane where high-energy emission has been detected in the X-ray, GeV and TeV gamma-ray bands. Past observations suggest IC 443 has been interacting with surrounding interstellar matter. Proximity between dense shocked molecular clouds and GeV–TeV gamma-ray emission regions detected by *EGRET*, *MAGIC* and *VERITAS* suggests an interpretation that cosmic-ray (CR) particles are accelerated by the SNR. With the high gamma-ray statistics and broad energy coverage provided by the LAT, we accurately characterize the gamma-ray emission produced by the CRs accelerated at IC 443. The emission region is extended in the energy band with $\theta_{68} = 0.27^\circ \pm 0.01^\circ(\text{stat}) \pm 0.03^\circ(\text{sys})$ for an assumed 2-dimensional Gaussian profile and overlaps almost completely with the extended source region of *VERITAS*. Its centroid is displaced significantly from the known pulsar wind nebula (PWN) which suggests the PWN is not the major contributor in the present energy band. The observed spectrum changes its power-law slope continuously and continues smoothly to the *MAGIC* and *VERITAS* data points. The combined gamma-ray spectrum ($200 \text{ MeV} < E < 2 \text{ TeV}$) is reproduced well by decays of neutral pions produced by a broken power-law proton spectrum with a break around 70 GeV.

1 *Subject headings:* gamma-rays: general, supernovae: individual (IC 443)

2 1. Introduction

3 IC 443 is a well-studied supernova remnant (SNR), possessing strong molecular line emission
 4 regions that make it a case for a SNR interacting with molecular clouds. The SNR is one of the best
 5 candidates for revealing the connection among SNRs, molecular clouds and high-energy gamma-ray
 6 sources as reviewed by Torres et al. (2003).

7 IC 443 is located in the outer Galactic plane and listed as a core-collapse supernova remnant
 8 (SNR), G189.1+3.0, in Green’s catalog (Green 2004). The SNR has an angular extent of $\sim 45'$ in the
 9 radio with a complex shape consisting of two half-shells with different radii (Shells A and B) (e.g.,
 10 Fesen & Kirshner 1980; Braun & Strom 1986a,b; Petre et al. 1988; Furst et al. 1990; Leahy 2004,
 11 and references therein). Its age is uncertain: some analyses indicate a young age (3 – 4 ky) (e.g.,
 12 Petre et al. 1988; Troja et al. 2008) but others indicate that it is older (20 – 30 ky) (e.g., Lozinskaya
 13 1981; Chevalier 1999; Olbert et al. 2001; Gaensler et al. 2006; Bykov et al. 2008; Lee et al. 2008).
 14 Its distance has not been measured directly but is assumed to be ~ 1.5 kpc, the distance to the Gem
 15 OB1 association to which the SNR belongs (e.g., Woltjer 1972; Olbert et al. 2001; Welsh & Sallmen
 16 2003; Gaensler et al. 2006). A pulsar wind nebula (PWN), CXOU J061705.3+222127, has been
 17 found in the southern periphery of the SNR but its association with the SNR has not yet been
 18 firmly established (Keohane et al. 1997; Olbert et al. 2001; Bocchino & Bykov 2001; Leahy 2004;
 19 Gaensler et al. 2006; Troja et al. 2008). To this day pulsation has not been reported at the position
 20 of the putative pulsar.

1 A general picture has been drawn from past observations and analyses that a variety of dy-
2 namical processes are taking place in the complex structure of IC 443 (e.g., Troja et al. 2006;
3 Lee et al. 2008; Troja et al. 2008, and references therein). The processes include: interaction of
4 SNR shocks with molecular and atomic clouds of various densities which produced a break-out
5 (Shell B) from Shell A as well as associated small-scale structures; interaction of the half-shells
6 with another SNR G189.6+3.3 (e.g., Asaoka & Aschenbach 1994; Keohane et al. 1997); penetra-
7 tion of shock fronts into dense molecular clouds leading to molecular line emission (e.g., Denoyer
8 1979a,b; Denoyer & Frerking 1981; Huang et al. 1986; Burton et al. 1988; van Dishoeck et al. 1993;
9 Richter et al. 1995; Chevalier 1999; Hewitt et al. 2006); and interaction between the PWN and the
10 environment (Olbert et al. 2001; Leahy 2004; Gaensler et al. 2006; Troja et al. 2008).

11 Of special interest for this study are the detections of high and very high energy (VHE) gamma
12 rays in the IC 443 vicinity. EGRET detected a gamma-ray source above 100 MeV, co-spatial ¹
13 with the SNR (3EG J0617+2238) (Sturmer & Dermer 1995; Esposito et al 1996; Lamb & Macomb
14 1997; Hartman et al 1999). The MAGIC telescope discovered a VHE source, MAGIC J0616+225
15 (Albert et al. 2007) which is displaced with respect to the position of the EGRET source, and
16 co-spatial with what appears to be the most massive molecular cloud in the neighborhood de-
17 tected in ¹²CO and ¹³CO emission lines (Burton et al. 1988; Dickman et al. 1992; Dame et al.
18 2001; Seta et al. 1998). *VERITAS* has confirmed the VHE emission (VER J0616.9+2230) and re-
19 solved the source to be extended (Acciari et al. 2009). The centroids of these 3 gamma-ray sources
20 are displaced from that of the PWN.

21 The LAT data for IC 443 provide an exciting opportunity to study the interaction of an SNR
22 with the interstellar medium, cosmic-ray (CR) acceleration and subsequent injection to the Galactic
23 space. The entire Milky Way has been deeply observed by the LAT and modeling of the diffuse
24 emission thereon allows the emission associated with IC 443 (the “IC 443 contribution”) to be
25 considered separately from the underlying Galactic diffuse emission, which has contributions from
26 inverse Compton scattering of CR electrons (the “Galactic IC component”) and CR electron and
27 proton interactions with interstellar nuclei (the “Galactic CR contribution”). In the LAT data
28 the spatial extension of the contribution from IC 443 can be measured along with its broad-band
29 spectrum

30 This paper is organized in the following sections: A brief description of the observation, event
1 reconstruction and gamma-ray selection is given in section 2. The analysis procedure is explained
2 in section 3 including the instrument response function (IRF) and separation of the Galactic CR
3 contribution, Galactic IC contribution, extragalactic emission and instrumental background. We
4 present results on the spatial extension and spectrum of the IC 443 contribution in section 4.
5 Discussion is given in section 5 and the paper is concluded in section 6.

¹We assume that the gamma-ray sources detected in the region are associated with locally accelerated CRs based on the spatial overlap with the IC 443 structure seen in the radio, IR, optical and X-ray bands.

2. Observations, Event Reconstruction and Gamma-Ray Selection

2.1. Observation in the Survey Mode

The *Fermi Gamma-ray Space Telescope*, launched on 11 June 2008, has been surveying all sky with the Large Area Telescope (LAT) since August 2008. Its wide field of view (~ 2.4 sr), large effective area (~ 8000 cm² at > 1 GeV), the improved point spread function (PSF)² ($\theta_{68}^{psf} \sim 0.6^\circ/0.9^\circ$ at $E = 1$ GeV) and the broad energy coverage (20 MeV – 300 GeV) bring much improved sensitivity and gamma-ray statistics over its predecessor *EGRET* (Atwood et al. 2009).

The LAT is a pair-conversion telescope where a gamma-ray is converted to an e^+e^- pair. Their trajectories are recorded in the tracker and the subsequent shower development are sampled both in the tracker and calorimeter. The tracker is surrounded by a segmented anti-coincidence detector which is used to reject events induced by charged CRs (Atwood et al. 2009; Abdo et al. 2009a). The LAT PSF (θ_{68}^{psf}) is determined at lower energies by multiple scattering in the tracker. At higher energies the PSF approaches to the limit given by the granularity of the tracker channels: it is $0.16^\circ/0.26^\circ$ at 5 GeV and $0.11^\circ/0.15^\circ$ at 10 GeV (Atwood et al. 2009).

The LAT was operated in the nominal all-sky survey during the present observation. In the observation the instrument axis was tilted from the zenith toward the orbit's north and south poles by 35 deg or 39 deg on alternate orbits to make sky coverage uniform. The trigger rate, mostly on cosmic rays, was ~ 2.2 kHz in average and varied between the maximum of ~ 5.0 kHz and the minimum of ~ 1.6 kHz dependently on the geomagnetic cut-off rigidity. On-board filtering reduced the event rate to ~ 450 Hz for the downlink. Data taking is disabled during passages through the South Atlantic Anomaly (Abdo et al. 2009a).

2.2. Gamma-ray Selection

Gamma-ray candidates are defined in 3 classes on the gamma-ray probability, background expected in orbit, current knowledge of the astronomical gamma-ray fluxes, and performance of the LAT. The *Diffuse* class has the tightest background rejection of the three (Atwood et al. 2009). However the effective area becomes small and strongly dependent energy below 200 MeV. The averaged rate for the *Diffuse* class event was ~ 0.6 Hz during the observation.

In the survey mode the Earth limb, an extremely bright source of gamma-rays, comes near the edge of the field of view. We have removed these gamma-rays with the reconstructed zenith angles

²The PSF is significantly different for gamma rays detected in the front and back portions of the tracker described in this section: the first and second of the two values separated by / are for those detected in the front and back, respectively. We use θ_{68} and θ_{95} with superscripts *psf*, *error* and *ext* to quantify the PSF, source localization error and source extension, respectively. The integrated probabilities in the 2-dimensional angular radii of θ_{68} and θ_{95} are 68% and 95%, respectively. For a symmetric 2D Gaussian distribution θ_{95} is $1.62 \times \theta_{68}$.

5 greater than 105° .

6 Cosmic-ray induced background in the *Diffuse* class becomes comparable in intensity to gamma-
7 rays from the IC 443 region at energies below 100 – 200 MeV and above 50 – 100 GeV. The back-
8 ground consists of residual cosmic rays misclassified as gamma rays and cosmic rays that convert
9 in the passive material just outside of the LAT without leaving a signal in the anti-coincidence
10 detector. We limit the energy range of this analysis between 200 MeV and 50 GeV where the
11 effective area and the instrumental background is best understood³.

12 The data analyzed here were obtained between 4 August 2008 and 4 July 2009. The gamma
13 rays in the circular region-of-interest (ROI) of radius 15° centered at the best-fit centroid of the
14 IC 443 contribution to be determined in section 4.1 ($\ell = 189.05^\circ$, $b = 3.03^\circ$) are selected for later
15 analyses. We refer to this set of events as the data set: the key selections described here are
16 summarized in Table 1.

17 Events in the data set are binned in energy at 13 logarithmic steps of 0.184 starting from
18 200 MeV. The matching energy-dependent exposure is calculated based on the orbit location, point-
19 ing direction, orientation and live-time accumulation of the LAT. The intensity is then calculated
20 by dividing maps of counts with maps of exposure in each energy bin.

21 3. Analysis Procedure

22 The present analysis focuses on determination of the centroid and extension of the IC 443 con-
23 tribution after separation of the Galactic CR contribution in the region. The latter will reflect the
24 detailed spatial structure of the molecular clouds through pionic and bremsstrahlung interactions
25 and potentially can be mistaken as a part of the IC 443 contribution. The uniform all-sky coverage
26 of the LAT observation allows us to isolate the IC 443 contribution cleanly from all Galactic-scale
27 contributions and determine its extension accurately. The *Sourcelike* analysis has been designated
28 specifically for this kind of analyses. Spectral analysis has been done with the LAT Science Tool
1 *gtlike*⁴ and has been cross-checked by *Sourcelike*. We give a brief description of the Instrument
2 Response Function (IRF) and *Sourcelike* before proceeding to the fitting.

³We are currently developing an improved event classification procedure to retain higher effective area at lower energies and to reduce background contaminations in the entire energy range.

⁴Available from <http://fermi.gsfc.gov/ssc/data/access/lat/BackgroundModels.html>, the Fermi Science Support Center url for the Science Tools.

3.1. Instrument Response Function

4 The spatial extension and spectral features of the gamma-ray emission are studied by com-
 5 paring the observation with predictions of source models. Predictions are made by convolving the
 6 spatial distribution and spectrum of the source models with the IRF and the exposure for the
 7 observation.

8 The IRF describes the overall performance of the instrument, event reconstruction and gamma-
 9 ray selection. In the *Fermi* LAT it has been formulated, before the launch, using an instrument
 10 simulation program (Atwood et al. 2009). The simulation program has been calibrated against
 11 beam test results (Atwood et al. 2009; Abdo et al. 2009a) and the predicted IRF has been validated
 12 on several bright point sources in the early operation phase.

13 The variation in the trigger rate results in variation in the fraction of the trigger-enabled time
 14 (the “live-time fraction”) between $\sim 94.3\%$ to $\sim 81.5\%$. Besides lowering the live-time fraction and
 15 the exposure, CR hits overlaid on a genuine gamma-ray track can reduce reconstruction efficiency
 16 and lead to incorrect event selection. The overall inefficiency has been found to scale linearly with
 17 the loss in the live-time fraction with a coefficient that depends on energy. The IRF used in the
 18 analysis, IRF P6_V3_Diffuse, has been corrected for inefficiency by, for example, $+23\%$, $+16\%$
 19 and $+12\%$ at 200 MeV, 500 MeV and 1 GeV, respectively.

3.2. Extension Analysis with *Sourcelike*

21 The intensity distribution observed by LAT from the IC 443 region is shown in Fig. 1 for a
 22 lower (1 – 5 GeV) and a higher (5 – 50 GeV) energy bands for an area of $8^\circ \times 8^\circ$ centered at $(\ell,$
 23 $b) = (189^\circ, 3^\circ)$ with 0.1° pixelization. Spatial extension of the IC 443 contribution is determined
 24 on the intensity distribution using *Sourcelike*, an analysis tool developed by the LAT team. In
 25 the tool, likelihood fitting is iterated to the data set assuming spatial source models and a spatial
 26 background model: we use combination of a symmetric 2D Gaussian source model or a point-source
 27 model and the standard background model.

28 The standard background model used in *Sourcelike* is formulated by summing the Galactic
 29 CR contribution, Galactic IC contribution and isotropic component⁵ given in the diffuse emission
 30 model⁶: it is referred as the background here after. All bright sources detected with the LAT
 31 (Abdo et al. 2009b) within 15° of the the centroid are included in the background.

1 The fit is performed for the entire data in the user-determined energy range. Absolute nor-
 2 malization of individual background components can be constrained or unconstrained in the fit: we

⁵The sum of the extragalactic background, unresolved sources and instrumental background: its spatial distribu-
 tion is assumed to be isotropic.

⁶*gll_iem_v02.fits* and *isotropic_iem_v02.txt* available from the url given in footnote 4.

3 leave the diffuse emission model as one unconstrained component and so are all bright sources in the
 4 ROI in the *Sourcelike* fit. The difference in Test Statistic (TS) values between the best-fit Gaussian
 5 distribution and the best-fit point-source which is $2\Delta\log(\text{Likelihood})$ gives a measure of statistical
 6 significance of the extension. We refer to this difference as TS_{ext} in this paper.

7 The ROI is energy dependent in the *Sourcelike*: 15° at 200 MeV and shrinks to a minimum
 8 of 3.5° at 50 GeV, which is at least a factor of 20 larger than θ_{68}^{psf} of the LAT at the same energy
 9 and more than a factor of 10 larger than the spatial extension (θ_{68}^{ext}) of the source to be determined
 10 later.

11 4. The IC 443 contribution

12 4.1. Spatial Extension of the IC 443 Contribution

13 Two energy bands, $1 \text{ GeV} < E < 5 \text{ GeV}$ (the lower energy band) and $5 \text{ GeV} < E < 50 \text{ GeV}$ (the
 14 higher energy band) have been selected to study the spatial extension of the IC 443 contribution.
 15 *Sourcelike* has been run for events in the two energy bands separately as well as in the combined
 16 energy band under a 2D Gaussian and point source hypotheses. The best-fit results are summarized
 17 in Table 2.

18 The number of gamma rays in the fitted Gaussian distribution is 4972 for $200 \text{ MeV} < E < 1 \text{ GeV}$,
 19 1597 for $1 \text{ GeV} < E < 5 \text{ GeV}$ and 236 for $5 \text{ GeV} < E < 50 \text{ GeV}$. For a given PSF, the accuracy of cen-
 20 troid determination is predicted to improve proportionally to the inverse of the square-root of the
 21 number of events. The accuracy quoted in Table 2 is consistent with this prediction for the effective
 22 PSF averaged over events in the energy bands $1 \text{ GeV} < E < 5 \text{ GeV}$ and $5 \text{ GeV} < E < 50 \text{ GeV}$.

23 The difference in TS (TS_{ext}) between the symmetric 2D Gaussian and point hypotheses is
 24 $+106$ to $+121$ (10.3 to 11.0σ)⁷ for the $1 - 5 \text{ GeV}$ band and $+212$ to $+81$ (14.6 to 9.0σ) for
 25 the $5 - 50 \text{ GeV}$ band. The centroids for the two bands are consistent within 0.04° . The IC 443
 26 contribution is extended to $\theta_{68}^{ext} = 0.26^\circ - 0.27^\circ$ in the two energy bands. The centroid in the high
 27 energy band is displaced southwards by $\sim 0.04^\circ$ ($\sim 1.5\sigma$) in the Galactic coordinate from that in
 28 the low energy band.

29 The results on source location and extension are robust: TS values have been examined at
 30 discrete points offset from the best-fit location and extension to confirm the fit. To verify the fit
 31 further, we have generated 100 simulated sets of events assuming the best-fit centroid, extension and
 1 background with the LAT Science Tool *gtobssim*. The simulated data are then processed through
 2 *Sourcelike* under 2D Gaussian and point source hypotheses. The distribution of TS_{ext} between the
 3 two hypotheses is consistent with the values given in Table 2.

⁷The two TS_{ext} values quoted are: the first one for that used in P6_V3_diffuse; and the second one for a worst-case PSF to be used later in section 5 to obtain a conservative systematic error.

4 The point source hypothesis is rejected at $TS_{ext} > 81$ or $> 9 \sigma$ independently in the two energy
 5 bands and at $TS_{ext} > 212$ or $> 14 \sigma$ in the combined energy band. The extensions in the two energy
 6 bands are mutually consistent within the errors given in Table 2.

7 The radial profiles of event distribution around the centroid is shown in Fig. 2 for the low and
 8 high energy bands together with the profile predicted for the point source hypothesis which is the
 9 LAT PSF weighted with the spectral distribution of the events *Sourcelike* has associated with the
 10 source under the point-source hypothesis.

11 Extension was poorly determined for $E=200$ MeV – 1 GeV because of the large PSF of the
 12 LAT in the energy range (Atwood et al. 2009). However, the centroid and extension are consistent
 13 with the extension determined above 1 GeV and given in Table 2. Hence we assume the same 2D
 14 Gaussian distribution in the entire energy range.

15 4.2. Spectrum of the IC 443 Contribution

16 The spectrum of the IC 443 contribution is fitted by the Science Tool *gtlike*, the *Fermi* standard
 17 tool, as well as by *Sourcelike*. In *gtlike*, we have to assume a spatial template for all spectral
 18 components included in the fitting. The data set is assumed to be a sum of three contributions:
 19 the best-fit 2D Gaussian distribution given for the $E = 1-50$ GeV range in Table 2 which represents
 20 the IC 443 contribution⁸; the background whose spatial distribution is represented by the sum of
 21 *gll_iem_v02.fit* and *isotropic_iem_v02.txt*; and the bright sources listed in Abdo et al. (2009b) in the
 22 square region of $8^\circ \times 8^\circ$ centered at the best-fit centroid ($\ell = 189.05$, $b = 3.03$).

23 The fitted IC 443 spectra from *gtlike* and *Sourcelike* agree well within the total error. We
 24 adopt the spectrum obtained with *gtlike* and tabulate in Table 3. It is converted to the spectral
 25 energy density (SED) and shown by circles with error bars in Fig. 3. Squares with error bars in the
 26 figure is the background spectrum normalized to the solid angle subtended by $\theta_{95}^{ext} = 0.45^\circ$ around
 27 the centroid given in Table 2. The IC 443 contribution is approximately 20 times higher than the
 28 background in the entire energy band.

29 The SED of the IC 443 contribution thus determined has been fitted with a single power-law
 30 and broken-power-law models: the results are tabulated in Table 4. The single power-law fit fails
 1 to represent the spectrum giving a large reduced chi-square of ~ 9 while the broken power-law
 2 fit represents the overall shape quite well giving a small reduced chi-square (~ 1.0) as shown in
 3 Table 4. The SED of the IC 443 contribution is plotted with those from previous observations,
 4 *EGRET* (Esposito et al 1996), *MAGIC* (Albert et al. 2007) and *VERITAS* (Acciari et al. 2009) in
 5 Fig. 4.

⁸The extension could not be determined at a high statistical significance for $E = 200$ MeV – 1 GeV but the spatial distribution of gamma rays is consistent with those given in Table 2.

4.3. Systematic error in determination of the centroid, extension and spectrum

When we determine the centroid of the IC443 contribution, uncertainty in the spatial distribution of the Galactic diffuse emission adds to the systematic error. The spatial template is taken from the standard diffuse emission model, *gll_iem_v02.fit*. To confirm our analysis, we have fitted the data set with the standard version of GALPROP for *Fermi* LAT (GALDEF 54_59Xvarh8S) (Strong & Moskalenko 1998; Strong et al. 2001, 2009) made of the CO line survey by Dame et al. (2001) and H I survey by Kalberla et al. (2005) as well as with a gas model made of the A_V map by Dobashi et al. (2005) and H I survey by Kalberla et al. (2005). The two alternate gas models have given centroids consistent with that given in Table 2.

The residual misalignment of the LAT and the star tracker can also contribute to the systematic error: the source localization has been verified on orbit using bright point sources to ± 30 arc-sec as of August 2009. The combination of all errors described here gives the overall systematic localization error in Table 5.

Our flux measurement depends on the knowledge on the effective area as a function of gamma-ray energy. We estimate systematic error in the effective area to be 10 %, 5 %, and 20 % at $E=100$ MeV, 562 MeV and > 10 GeV respectively.

Uncertainty in the background used in *gtlike* and *Sourcelike* can also introduce error in the flux measurement. This uncertainty is estimated to be $\sim 20\%$ for 200 MeV – 1 GeV and $\sim 30\%$ for > 1 GeV of the background (Abdo et al. 2009c,d). Systematic error at each energy bin is determined through a linear interpolation in $\log_{10}(E)$ among the values quoted above.

The PSF used in this analysis has been derived on the detector simulation which was itself verified in accelerator tests (Atwood et al. 2009). As gamma-ray statistics improves, the PSF will be updated against measurement on bright point sources. In the present study, we have used a preliminary upper limit to assess possible systematic error introduced by inaccurate formulation of PSF: we consider this as the “worst-case” PSF. The worst-case PSF (θ_{68}^{psf}) gives a widest limit while the for $E > 5$ GeV is about 40% larger than the default PSF. The source centroid comes out to be consistent within the total error when *Sourcelike* is run with the worst-case PSF. We have included the difference in the systematic error given in Tables 2 and 5.

5. Discussion

The IC 443 system consists of a complex distribution of molecular and atomic clouds in the southern rim of Shell A (e.g., Snell et al. 2005; Lee et al. 2008, and references therein). Molecular clouds wrap around the southern rim and the boundary region between Shells A and B (Beichman et al. 1988; Seta et al. 1998; Dickman et al. 1992; Dame et al. 2001). Molecular lines from shocked gas have been found in several clouds suggesting interaction with the blast-wave at multiple sites (e.g., Cornett et al. 1977; Denoyer & Frerking 1981; Huang et al. 1986; Burton et al.

7 1988; Dickman et al. 1992; van Dishoeck et al. 1993; Richter et al. 1995; Seta et al. 1998; Snell et al.
 8 2005). A prominent band of HI gas has also been found in the southeastern part of Shell A (Denoyer
 9 1978; Giovanelli & Haynes 1979; Lee et al. 2008, and references therein.). Some parts of the H I
 10 gas are found to be shocked (Braun & Strom 1986a; Lee et al. 2008).

11 The total mass of the molecular gas in the region is estimated to be $\sim 1 \times 10^4 M_{\odot}$ (Torres et al.
 12 2003), of which only a small fraction is shocked (Snell et al. 2005). The total mass in the H I belt
 13 is estimated at $\sim 730 M_{\odot}$ of which $\sim 500 M_{\odot}$ is shocked (Lee et al. 2008). Despite past extensive
 14 observations and analyses, little is known about how the multiple shell-like structures are spatially
 15 correlated and where one or more supernova explosions took place.

16 In the group of shocked molecular clouds schematically shown in Fig. 5, Cloud G⁹ lies closest to
 17 the centroid of the *MAGIC* and *VERITAS* sources (Huang et al. 1986). It appears to be extended
 18 by $\sim 8'$ and overlaps with a non-shocked CO cloud formation (Huang et al. 1986; Burton et al.
 19 1988; Dickman et al. 1992). Chevalier (1999) has suggested that interaction between Shell A and
 20 Cloud G is responsible for the gamma-ray emission observed by *EGRET*. Existence of an OH
 21 Maser in the cloud suggests that the densities reach $\sim 10^4 \text{ cm}^{-3}$ (Frail et al. 1996; Hewitt et al.
 22 2006, 2008). A later CO line observation by Snell et al. (2005) found a compact core of extension
 23 $\sim 1' - 2'$ in Cloud G at ($\ell = 189.03^{\circ}$, $b = 2.90^{\circ}$). Fainter maser emission has also been found in
 24 Clouds B and D at ($\ell = 189.18^{\circ}$, $b = 2.97^{\circ}$) and ($\ell = 189.25^{\circ}$, $b = 3.13^{\circ}$), respectively (Hewitt et al.
 25 2006, 2008).

26 The locations and extensions of the gamma-ray emission from IC 443 detected by *EGRET*
 27 (Hartman et al 1999), *MAGIC* (Albert et al. 2007), *VERITAS* (Acciari et al. 2009), and *Fermi*
 28 LAT are summarized in Table 5 and shown in Fig. 5. *Fermi* LAT gives the best source localization
 29 or the smallest error circle (θ_{68}^{error}) for the 2D Gaussian centroid (0.03°) and a precise determination
 30 of the source extension ($0.27^{\circ} \pm 0.01^{\circ}(stat) \pm 0.03^{\circ}(sys)$). Our centroid determined for $1 \text{ GeV} <$
 31 $E < 50 \text{ GeV}$, ($\ell = 189.05^{\circ}$, $b = 3.03^{\circ}$), is 0.05 deg away from the *EGRET* source (3EG J0617+2238)
 1 but within θ_{95}^{error} of their localization error; 0.15 deg from the *MAGIC* source (J0610+225) which
 2 is at more than 5 times their localization error (θ_{68}^{error}); and 0.12 deg from the *VERITAS* source
 3 (VER J0616.9+2230) or at 1.5 times their localization error (θ_{68}^{error}).

4 The measured source extension, $\theta_{68}^{ext} = 0.27^{\circ} \pm 0.01^{\circ}(stat) \pm 0.03^{\circ}(sys)$, is comparable with
 5 $\theta_{68}^{ext} = 0.24^{\circ} \pm 0.05^{\circ}(stat) \pm 0.06^{\circ}(sys)$ ¹⁰ given by *VERITAS*. The two extended regions overlap
 6 almost completely. The three shocked clouds with OH maser (Clouds B, D and G) are within our
 7 measured extension and so are other shocked clouds (Clouds C, E, F and H). The PWN localized
 8 at ($\ell = 189.227^{\circ}$, $b = 2.897^{\circ}$) by Olbert et al. (2001) and Gaensler et al. (2006) is 0.26 deg away
 9 from our centroid but within our measured extension θ_{68}^{ext} .

10 The *Fermi* spectrum of the IC 443 contribution shown in Fig. 3 is flat between a few 100 MeV

⁹Labeling is given by Denoyer (1979b); Huang et al. (1986).

¹⁰We assume the extension is modeled by a symmetric 2D Gaussian and converted to $\theta_{68} = 1.51 \times \theta_{1\sigma}$.

11 and ~ 3 GeV, suggesting the origin being mostly neutral pions produced by protons ¹¹. The dashed
 12 line in the figure represents the gamma-ray spectrum expected from a $10^4 M_\odot$ cloud bombarded
 13 with the Galactic CR protons predicted at IC 443 scaled up by a factor of 100. The Galactic
 14 CR spectrum is taken from the standard GALPROP (54_59Xvarh8S) (Strong & Moskalenko 1998;
 15 Strong et al. 2001, 2009) and the parameterized cross-section for $pp \rightarrow \gamma$ by Kamae et al. (2006).
 16 In GALPROP the Galactic CR proton spectrum depends on the radius from the Galactic Center
 17 and the displacement from the Galactic Plane. The spectrum at the radius of IC 443 is $\sim 10\%$
 18 lower than that in the solar vicinity and has a power-law shape with index ~ 2.7 .

19 The *Fermi* SED is compared with those of *EGRET MAGIC* and *VERITAS* in Fig. 4. The
 20 *EGRET* spectrum is consistent with our spectrum except for their 3 GeV point. *MAGIC* and
 21 *VERITAS* do not overlap with the LAT in the energy coverage. Their fluxes are consistent with
 22 ours if extrapolated down to ~ 50 GeV by assuming their measured power-law indices.

23 Since the source regions of *Fermi* LAT and *VERITAS* overlap within their respective uncer-
 24 tainties listed in Table 5, we can judiciously proceed to fit the 2 spectra with one spectral model.

25 On the assumption that the distance is $d = 1.5$ kpc, the isotropic luminosity of IC 443 inte-
 26 grated over the energy band (0.2 – 50 GeV) is 1.2×10^{35} erg/s. Electron bremsstrahlung can hardly
 27 explain the observed IC 443 gamma-ray emissivity: the cross-sections for bremsstrahlung and pionic
 28 gamma-ray emission are similar in the present energy band, so the bremsstrahlung-to-pion ratio is
 29 approximately the ratio of CR electron and proton fluxes which is ~ 0.01 . The observed gamma-ray
 30 flux is too high for bremsstrahlung to be the dominant process. Inverse Compton scattering can
 31 not explain the observed IC 443 gamma-ray emission either: the gas density of the emission region
 32 is $\sim 50 - 100 \text{ cm}^{-3}$ and the Compton-to-bremsstrahlung ratio is $\sim 0.01 - 0.001$ for the seed photon
 33 density of the cosmic microwave background. We note that there is no bright source of seed photons
 34 known in the region of the IC 443 contribution. The gamma-ray energy will be strongly bound by
 35 the electron spectrum which likely rolls down similarly as the proton spectrum. Our observation,
 36 however, does not rule out a small contribution from bremsstrahlung near the minimum of the
 37 present energy band.

38 In a hadronic scenario, the observed photon spectrum up to TeV energies can be well fitted
 1 by an underlying pion-producing proton population with a broken power-law spectrum $F_p(T_p) =$
 2 $5.9 \times 10^{-2} (T_p/69 \text{ GeV})^{-\alpha} (10^4 M_\odot/M_{gas}) \text{ cm}^{-2} \text{ s}^{-1} \text{ GeV}^{-1}$, where α is 2.09 ± 0.04 for $T_p < 69$ GeV
 3 and 2.87 ± 0.07 for $T_p > 69$ GeV respectively, and M_{gas} is the gas mass in the interaction region. The
 4 error (statistical) in the fitted break energy is ± 25 GeV and the chi-square for the best-fit broken
 5 power-law model is 9.6/14 per degree-of-freedom. Assuming the gas density ($n \text{ cm}^{-3}$) is uniform and

¹¹We include cosmic-rays and target nuclei heavier than the proton (the alpha particle and heavier nuclei) in protons throughout this paper. In the approximation we adopt here (Gaisser & Schaefer 1992), these can be accounted for by multiplying a nuclear factor (~ 1.7) without changing the CR proton spectrum. The known gamma-ray producing particle processes which do not go through neutral pions (e.g., $\eta^0 \rightarrow \gamma\gamma$ and direct photon production) contribute less than 1% in the present energy range.

6 the proton spectrum is the broken power-law everywhere in the interaction region, the total energy
7 of the interacting protons is given by $W_p(> 0.5 \text{ GeV}) = 5.6 \times 10^{48} (n/240 \text{ cm}^{-3})^{-1} (d/1.5 \text{ kpc})^2 \text{ erg}$.
8 Note that the pion production threshold is $\sim 0.5 \text{ GeV}$. Taking $M_{gas} \sim 10^4 M_\odot$ and a gas volume
9 ranging from $4\pi/3 \times (\theta_{68}^{ext} d)^3 = 5 \times 10^{58} \text{ cm}^3$ up to $4\pi/3 \times (\theta_{95}^{ext} d)^3 = 2 \times 10^{59} \text{ cm}^3$, we obtain n
10 $\sim 60 - 240 \text{ cm}^{-3}$, giving $W_p(> 0.5 \text{ GeV}) = (0.56 - 2.2) \times 10^{49} \text{ erg}$. We note that energies carried
11 by local nuclear cosmic rays outside of the interaction region and by local leptonic cosmic rays are
12 not included in the estimation. The fitted gamma-ray spectrum is shown in Fig. 3 and Fig. 4. We
13 note that inclusion of the *MAGIC* points in the fit does not change the above results.

14 Broad-band gamma-ray spectral models have been proposed assuming CR interaction with
15 interstellar gas in IC 443 by Torres et al. (2008) and Zhang & Fang (2008). Torres et al. (2008)
16 model the CR diffusion in the SNR to allow spectral differences in the protons interacting with
17 the ambient gas in the shell and in a detached molecular cloud. Zhang & Fang (2008) predict one
18 contribution to come from the SNR shell evolving in the interstellar matter and the other from CR
19 interaction with molecular clouds. One difference between the two models is that Zhang & Fang
20 (2008) include inverse Compton scattering as a possible emission mechanism.

21 The combined spectrum of *Fermi* and *VERITAS* gives a strong constraint to spectral models
22 for the IC 443 contribution. Since the spectrum of the dominant CR component (proton) is rolling
23 over at $\sim 70 \text{ GeV}$, secondary electrons and positrons can only contribute at energies $E_\gamma < 7 \text{ GeV}$.
24 This constrains the parameter space of the model by Zhang & Fang (2008). The overlap between
25 the *Fermi* and *VERITAS* spatial extensions and the smooth spectral transition from *Fermi* to
26 *VERITAS* constrain the parameter spaces of the models by Torres et al. (2008) and Zhang & Fang
27 (2008).

28 We discuss briefly about possible mechanisms behind the broken power-law form of the proton
29 spectrum deduced from the gamma-ray observation of IC 443. The most obvious one is escape of
30 highest energy CRs from the acceleration site. When accelerated CR protons exceed the maximum
31 energy determined by the magnetic field and linear-scale of the acceleration site, they escape into
32 the Galactic space. Theory of diffusive shock acceleration (DSA) assumes spherically symmetric
33 morphology and predicts the CR spectrum to roll over exponentially at the maximum energy. The
34 maximum energy depends on the condition of the acceleration site: Ptuskin & Zirakashvili (2005)
35 have incorporated various instabilities in DSA and predict the maximum energy as a function of the
36 SNR age. For the age of IC 443 ($\sim 30 \text{ kyr}$), the maximum proton energy can be around 100 GeV
37 (Fig.1 of Ptuskin & Zirakashvili 2005) or near the observed break energy ($\sim 69 \text{ GeV}$) beyond
38 which the spectrum is assumed to cut-off exponentially. We have fitted the observed gamma-ray
1 spectrum with a single power-law, exponentially cut off proton spectrum to get chi-square per
2 degree-of-freedom of 30.3/15 much higher than 9.6/14 for the broken power-law spectrum. This
3 simple statistical test therefore suggests that the observed broad-band gamma-ray spectrum is
4 inconsistent with the simple DSA-based CR escape scenario which predicts a simple powerlaw with
5 an exponential cutoff in the proton spectrum. We also note that DSA has mostly been studied for
6 uniform gas densities around 1 cm^{-3} , while the gas around IC443 is inhomogenous and in various

7 shocked molecular clouds around the remnant also denser.

8 Historically, after the discoveries of the *EGRET* source (Sturmer & Dermer 1995; Esposito et al
9 1996) and the hard X-ray source (Keohane et al. 1997) but before the discoveries of the PWN
10 (Olbert et al. 2001) and *MAGIC* source (Albert et al. 2007), models have been proposed to explain
11 the emission between ~ 5 keV and ~ 5 GeV by bremsstrahlung in dense clouds (e.g., Bykov et al.
12 2000) with possible mix of synchrotron (e.g., Sturmer et al. 1997). The SNR was also studied
13 as a part of non-linear shock evolution in various environments (e.g., Baring et al. 1999). While
14 their predictions for IC 443 are not supported by the later observations including the present one,
15 parameters in these studies can be readjusted to describe the bremsstrahlung contribution discussed
16 below.

17 The bremsstrahlung likely makes a non-negligible contribution below $E_\gamma = 200$ MeV where
18 the *EGRET* data points exceed the best-fit pionic spectrum (see Fig. 4). As our understanding of
19 the IRF and cosmic-ray-induced background improve, analysis will be extended to energies lower
20 than 200 MeV and the bremsstrahlung spectrum component will be determined accurately. The
21 hard X-ray SED measured by Beppo-SAX (Bocchino & Bykov 2000) is substantially higher than
22 that by XMM (Bocchino & Bykov 2001): which may suggest bremsstrahlung contribution near the
23 PWN location as has been discussed by Sturmer et al. (1997) and Bykov et al. (2000).

24 6. Conclusions

25 We have studied gamma-ray emission from the nearby SNR IC 443 (G189.1+3.0) using the
26 first 11 months of science data from *Fermi* LAT. The uniform sky coverage and high gamma-ray
27 statistics of the observation have enabled us to separate the genuine IC 443 contribution from the
28 emissions by Galactic CRs on interstellar gas, inverse Compton scattering by Galactic CR electrons
29 on large-scale interstellar radiation field, extragalactic sources and instrumental background.

30 Based on the extension study described in subsections 4.1 and the spectral analysis described
31 in subsection 4.2 as well as discussions given in section 5, we conclude that:

- 32 • The gamma-ray emission from IC 443 is detected at $\sim 86\sigma$ level: the emission is extended with
1 68% containment angular radius $\theta_{68}^{ext} = 0.27^\circ \pm 0.01^\circ \pm 0.03^\circ$ in the energy range between 1 GeV
2 and 50 GeV. The extension remains unchanged within error in the low ($1 \text{ GeV} < E < 5 \text{ GeV}$)
3 and high ($5 \text{ GeV} < E < 50 \text{ GeV}$) energy bands.
- 4 • The centroid of the emission moves at $\sim 1 - 1.5\sigma$ level toward that of the *VERITAS* source as
5 the energy band changes from 1 – 5 GeV to 5 – 50 GeV. The centroid is inconsistent with the
6 PWN location, suggesting that the PWN is not the major contributor in the present energy
7 range.
- 8 • The centroid of the emission is consistent with that of *EGRET* (3EG J0617+2238), dis-

9 placed more than $5 \times \theta_{68}^{error}(MAGIC)$ from that of *MAGIC* (J0610+225), and at $1.5 \times$
10 $\theta_{68}^{error}(VERITAS)$ that of *VERITAS* (VER J0616.9+2230).

- 11 • The extended source region overlaps almost completely that of *VERITAS*. A group of molecu-
12 lar clouds (Clouds B, C, D, F, and G), the SNR shell and the PWN are within the overlapping
13 region (θ_{68}^{ext}), leaving possibility that some or all of them contribute to the observed emission.
- 14 • The SED can not be represented by a single power-law but is consistent with a broken power-
15 law with a break at $E_\gamma = 3.25 \pm 0.6$ GeV.
- 16 • The SED has a broad peak between a few 100 MeV and ~ 5 GeV which is consistent with the
17 majority of the emission coming from neutral pion decays. For the emission being hadronic
18 originating from a single proton population, the underlying proton spectrum is consistent
19 with a broken power-law shape (chi-square per degree-of-freedom of 9.6/14) but not with an
20 exponential cut-off (30.3/15). For the estimated total mass of interacting gas of $10^4 M_\odot$, the
21 total energy in the pion-producing protons is estimated to be $(0.56 - 2.2) \times 10^{49}$ erg.

22 Higher statistics is needed to establish association or non-association of the gamma-ray emis-
23 sion with the molecular clouds and/or the PWN as well as CR injection process from the SNR into
24 the Galactic space. Identification of the emission mechanisms and underlying CR spectra effective
25 in individual sites will follow after such studies.

26 *Fermi* LAT is expected to accumulate needed statistics well within the planned mission lifetime.

27 *Acknowledgements*

28 The *Fermi* LAT Collaboration acknowledges generous ongoing support from a number of
29 agencies and institutes that have supported both the development and the operation of the LAT as
1 well as scientific data analysis. These include the National Aeronautics and Space Administration
2 and the Department of Energy in the United States, the Commissariat à l’Energie Atomique and
3 the Centre National de la Recherche Scientifique / Institut National de Physique Nucléaire et de
4 Physique des Particules in France, the Agenzia Spaziale Italiana and the Istituto Nazionale di Fisica
5 Nucleare in Italy, the Ministry of Education, Culture, Sports, Science and Technology (MEXT),
6 High Energy Accelerator Research Organization (KEK) and Japan Aerospace Exploration Agency
7 (JAXA) in Japan, and the K. A. Wallenberg Foundation, the Swedish Research Council and the
8 Swedish National Space Board in Sweden.

9 Additional support for science analysis during the operations phase is gratefully acknowledged
10 from the Istituto Nazionale di Astrofisica in Italy and the Centre National d’Etudes Spatiales in
11 France.

REFERENCES

- 13 Abdo, A. A., et al. 2009a, *Astropart. Phys.* (in press), arXiv:0904.2226
- 14 Abdo, A. A. et al. 2009b, *ApJS*, 183, 46
- 15 Abdo, A. A. et al. 2009c, *Phys. Rev. Lett.*, (submitted)
- 16 Abdo, A. A. et al. 2009d, *ApJ*, 703, 1249
- 17 Acciari, V. A., et al. 2009, *ApJ*, 698, L133
- 18 Albert, J., et al. 2007, *ApJ*, 664, L87
- 19 Asaoka, I. & Aschenbach, B. 1994, *A&A*, 284, 573
- 20 Atwood, W., et al. 2009, *ApJ*, 697, 1071
- 21 Baring, M. G., Ellison, D. C., Reynolds, S. P., Grenier, I. A., & Goret, P. 1999, *ApJ*, 513, 311
- 22 Beichman, C., et al. (eds.), 1988, *IRAS Catalogs and Atlases*, NASA RP-1190.
- 23 Bocchino, F. & Bykov A. M., 2000, *A&A*, 362, L29.
- 24 Bocchino, F. & Bykov A. M., 2001, *A&A*, 376, 248.
- 25 Braun, R., & Strom, R. G. 1986a, *A&AS*, 63, 345
- 26 Braun R. & Strom R. J. 1986b, *A&A*, 164, 193
- 1 Burton, M. G., Geballe, T. R., Brand, P. W. J. L., & Webster, A. S. 1988, *MNRAS*, 231, 617
- 2 Bykov, A. M., Chevalier, R. A., Ellison, D. C., & Uvarov, Y. A. 2000, *ApJ*, 538, 203
- 3 Bykov, A. M. et al. 2008, *ApJ*, 676, 1050
- 4 Chevalier, R. A. 1999, *ApJ*, 511, 798
- 5 Cornett, R. H., Chin, G., & Knapp, G. R. 1977, *A&A*, 54, 889
- 6 Dame, T., Hartmann, D., & Thaddeus, P. 2001, *ApJ*, 547, 792
- 7 Denoyer, L. K. 1978, *MNRAS*, 183, 187
- 8 Denoyer, L. K. 1979a, *ApJ*, 228, L41
- 9 Denoyer, L. K. 1979b, *ApJ*, 232, L165
- 10 Denoyer, L. K., & Frerking, M. A. 1981, *ApJ*, 246, L37
- 11 Dickman, R. L., Snell, R. L., Ziurys, L. M., & Huang, Y.-L. 1992, *ApJ*, 400, 203

- 12 Dobashi, K. et al. 2005 PASJ, 57, S1
- 13 Esposito, J. A., Hunter, S. D., Kanbach, G., & Sreekumar, P. 1996, ApJ, 461, 820
- 14 Fesen, R. A. & Kirshner, R. P. 1980, ApJ, 242, 1023
- 15 Frail, D. A., Goss, W. M., Reynoso, E. M., Giacani, E. B., Green, A. J., & Otrupcek, R. 1996, AJ,
16 111, 1651
- 17 Furst, E., Reich, W., Reich, P., & Reif, K. 1990, A&AS, 85, 691
- 18 Gaensler B. M. et al., 2006, ApJ, 648, 1037.
- 19 Gaisser, T. K., & Schaefer, R. K. 1992 ApJ, 394, 174
- 20 Giovanelli, R., & Haynes, M. P. 1979, ApJ, 230, 404
- 21 Green, D. A., 2004, BASI, 32, 335G.
- 22 Hartman, R. C. et al. 1999, ApJS, 123, 79
- 23 Hewitt, J. W. et al., 2006, ApJ, 652, 1288
- 24 Hewitt, J. W. et al., 2008, ApJ, 683, 18 Federman, S. R., Wallerstein, G., & Means, T. 2009, ApJ,
25 696, 1533
- 26 Huang, Y.-L., Dickman, R. L., & Snell, R. L. 1986, ApJ, 302, L63
- 27 Kalberla, P. M. W., et al. 2005, A&A, 440, 775
- 1 Kamae, T. et al. 2006, ApJ, 647, 692; Erratum 2007, ApJ, 662, 779
- 2 Keohane, J. W., Petre, R., Gotthelf, E. V., Ozaki, M., & Koyama, K. 1997, ApJ, 484, 350
- 3 Lamb, R. C., & Macomb, D. J. 1997, ApJ, 488, 872
- 4 Leahy, D. A. 2004, AJ, 127, 2277
- 5 Lee, Jae-Joon, et al. 2008, ApJ, 135, 796
- 6 Lozinskaya, T. A. 1981, Soviet Astron. Lett., 7, 17 & Bowyer, S. 1976, ApJ, 207, 894
- 495 Olbert, C. M., Clearfield, C. R., Williams, N. E., Keohane, J. W., & Frail, D. A. 2001, ApJ, 554,
496 L205
- 497 Petre, R., Szymkowiak, A. E., Seward, F. D., & Willingale, R. 1988, ApJ, 335, 215
- 498 Ptuskin, V. S., & Zirakashvili, V. N. 2005, A&A, 429, 755
- 499 Richter, M. J., Graham, J. R., & Wright, G. S. 1995, ApJ, 454, 277

- 500 Seta, M., et al. 1998, ApJ, 505, 286
- 501 Snell, R. L. et al., 2005 ApJ 620 758
- 502 Strong, A. W., & Moskalenko, I. V. 1998 ApJ., 509, 212
- 503 Strong, A. W., Moskalenko, I. V., & Reimer, O. 2001 ApJ, 537, 763
- 504 Strong, A. W., et al., 2009 arXiv:0907.0559
- 505 Sturmer, S. J., & Dermer, C. D. 1995, A&A, 293, L17
- 506 Sturmer, S. J., Skibo, J. G., Dermer, C. D., & Mattox, J. R. 1997, ApJ, 490, 619
- 507 Torres, D. F., Romero, G. E., Dame, T. M., Combi, J. A., & Butt, Y. M. 2003, Phys. Rep., 382,
508 303
- 509 Torres, D. F., Rodriguez Marrero A. Y., & de Cea del Pozo E. 2008, MNRAS Letters, 387, 59
- 510 Troja, E., Bocchino, F. & Reale, F. 2006, ApJ, 649, 258
- 511 Troja, E., Bocchino, F., Miceli, M., & Reale, F. 2008, A&A, 485, 777
- 512 van Dishoeck, E. F., Jansen, D. J., & Phillips, T. G. 1993, A&A, 279, 541
- 513 Welsh, B. Y., & Sallmen, S. 2003, A&A, 408, 545
- 514 Woltjer, L. 1972, ARA&A, 10, 129
- 515 Zhang, L. and Fang, J., 2008, ApJ, 675, L21

Table 1. Selection for the Data Set

Parameter	Value
Time Period (MET)	239557417 – 268416079
Energy Range	200 MeV - 50 GeV
ROI	$\leq 15^\circ$ in radius
Photon Class	<i>Pass 6 Diffuse</i>
Additional Cut	Zenith angle $\leq 105^\circ$

Table 2. Centroid and Extension of the IC 443 Contribution

Model	ℓ ($^\circ$)	b ($^\circ$)	θ_{68}^{error} ($^\circ$) ^a	θ_{68}^{ext} ($^\circ$) ^a	θ_{95}^{ext} ($^\circ$) ^a	TS_{ext} ^b
1 – 5 GeV						
Point Source	189.05	3.04	0.02	0
Gaussian	189.05	3.05	0.02	0.27 ± 0.03	0.44 ± 0.04	+106/ + 121
5 – 50 GeV						
Point Source	189.05	2.98	0.03	0
Gaussian	189.06	3.00	0.03	0.26 ± 0.04	0.42 ± 0.07	+81/ + 212
1 – 50 GeV						
Point Source	189.05	3.02	0.02	0
Gaussian	189.05	3.03	0.02	0.27 ± 0.03	0.45 ± 0.05	+212/ + 362

^aErrors of centroids and extensions quoted include systematic errors.

^bThe two values shown in this column are the lower and higher of the TS_{ext} obtained with the default PSF (the first) and worst-case PSF (the second) described in the text.

Table 3. Spectrum of the IC 443 Contribution

E_{center} [MeV]	dN/dE [$\text{cm}^{-2} \text{s}^{-1} \text{MeV}^{-1}$]	dN/dE (stat error)	dN/dE (sys error)
247.31	8.63×10^{-10}	4.80×10^{-11}	6.37×10^{-11}
378.19	4.11×10^{-10}	1.87×10^{-11}	2.52×10^{-11}
578.32	1.72×10^{-10}	7.81×10^{-12}	8.89×10^{-12}
884.36	8.31×10^{-11}	3.59×10^{-12}	6.11×10^{-12}
1352.34	3.25×10^{-11}	1.65×10^{-12}	3.12×10^{-12}
2067.96	1.51×10^{-11}	8.36×10^{-13}	1.78×10^{-12}
3162.27	5.81×10^{-12}	4.06×10^{-13}	8.14×10^{-13}
4835.67	2.40×10^{-12}	2.05×10^{-13}	3.90×10^{-13}
7394.58	7.49×10^{-13}	8.98×10^{-14}	1.38×10^{-13}
11307.60	2.80×10^{-13}	4.29×10^{-14}	5.61×10^{-14}
17291.30	9.13×10^{-14}	1.93×10^{-14}	1.82×10^{-14}
26441.41	2.95×10^{-14}	8.94×10^{-15}	5.90×10^{-15}
40433.51	6.46×10^{-15}	3.35×10^{-15}	1.29×10^{-15}

Table 4. Spectral Fit to the IC 443 Contribution

Model	γ_1	γ_2	E_{break} (GeV)	F_{200}^a ($10^{-7} \text{cm}^{-2} \text{s}^{-1}$)	χ^2/dof
IC 443 Broken PL	1.93 ± 0.03	2.56 ± 0.11	3.25 ± 0.6	2.85 ± 0.07	8.9/9
IC 443 PL	2.08 ± 0.02	3.00 ± 0.07	90/11

^aTotal flux integrated above 200 MeV obtained with *gtlike* assuming the best-fit broken power-law model and the best-fit 2D Gaussian spatial distribution.

Table 5. Summary of Locations and Extensions of the Gamma-Ray Sources

Observation	ℓ ($^\circ$)	b ($^\circ$)	θ_{68}^{error} of localization ($^\circ$)	θ_{68}^{ext} of extension ($^\circ$)
<i>EGRET</i>	189.00	3.05	0.13 (θ_{95}^{error})	N/A
<i>MAGIC</i>	189.03	2.90	± 0.025 (stat) ± 0.017 (sys)	N/A
<i>VERITAS</i>	189.07	2.92	± 0.03 (stat) ± 0.08 (sys)	0.24 ± 0.05 (stat) ± 0.06 (sys)
<i>Fermi</i>	189.05	3.03	± 0.01 (stat) ± 0.02 (sys)	0.27 ± 0.01 (stat) ± 0.03 (sys)

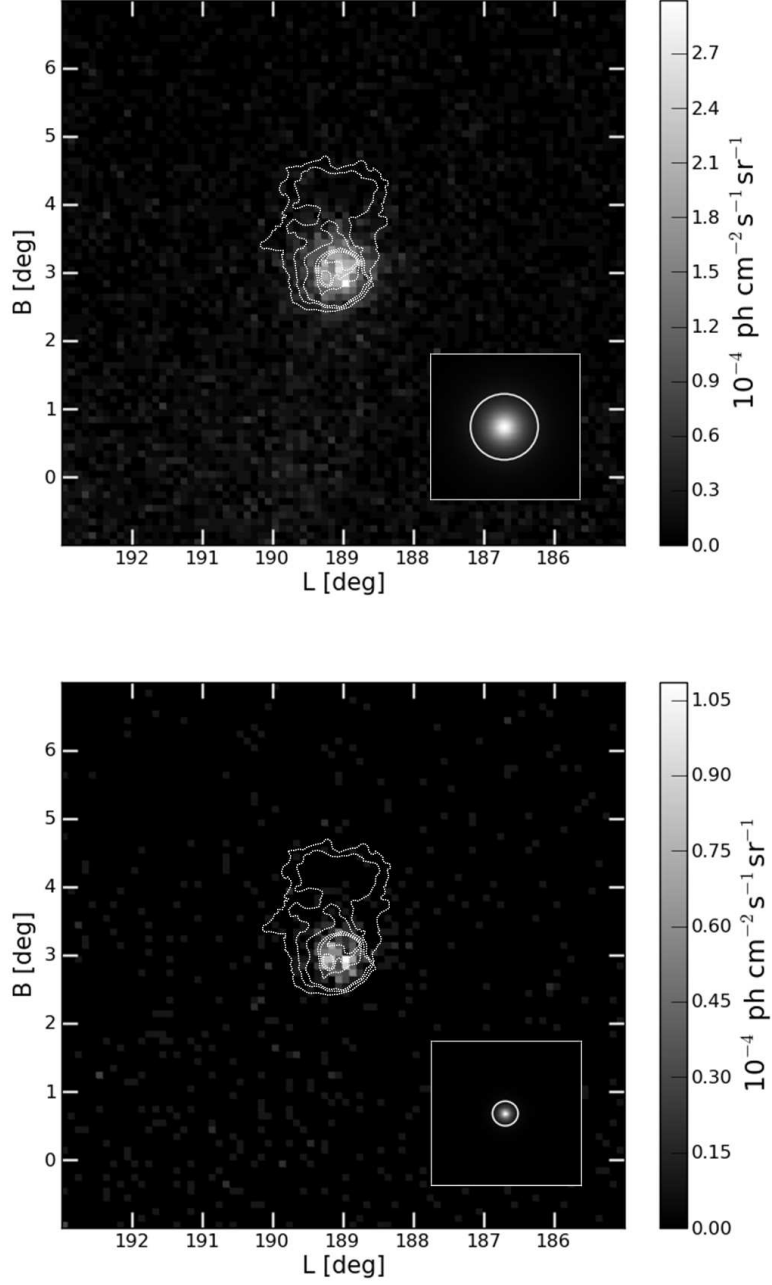


Fig. 1.— Intensity map of the IC 443 region in the 1 – 5 GeV (left) and 5 – 50 GeV (right) bands. Units of intensity are $10^{-4} \text{ cm}^{-2} \text{ s}^{-1} \text{ sr}^{-1}$ for the color scale. The overlay is the 2.7 GHz radio continuum contours taken from Furst et al. (1990). The insets are the spectrum-weighted LAT PSF for each energy band, with the white circles showing the corresponding θ_{68}^{psf} .

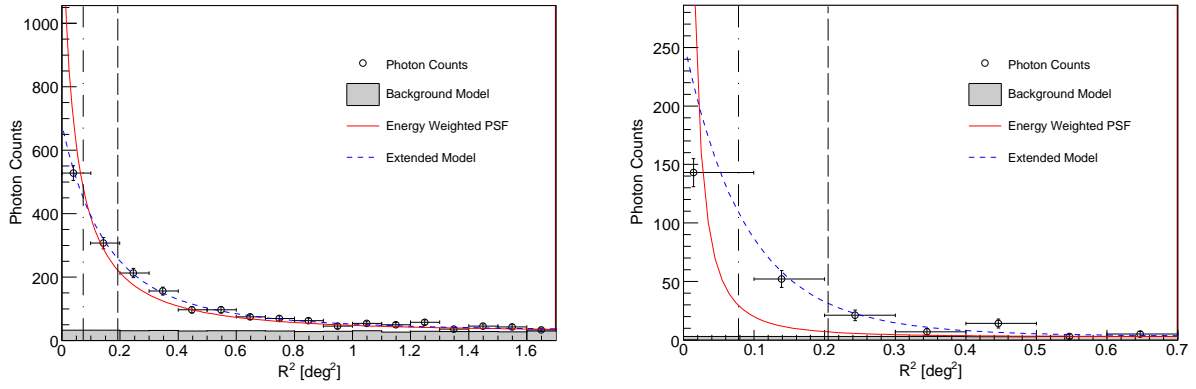


Fig. 2.— Radial profile of the gamma rays *SourceLike* associated with the IC 443 contribution (data points), compared with the effective spectrum-weighted LAT PSF (solid red line) and the fitted 2D Gaussian extended model (dashed blue line). The left and right panels correspond to the low (1 – 5 GeV) and high (5 – 50 GeV) energy bands, respectively. The points in the count profile are plotted at the weighted average radial positions within their respective bins. The vertical dash-dot and dashed lines correspond to the fitted extension θ_{68}^{ext} and θ_{95}^{ext} given in Table 2 for the respective energy bands.

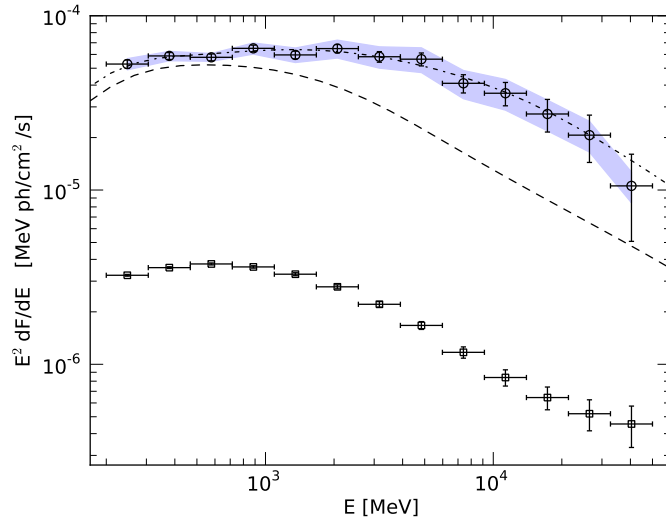


Fig. 3.— The gamma-ray spectrum of the IC 443 contribution: The upper and lower data points represent the IC 443 contribution and the total background, respectively. The background has been scaled to match the solid angle subtended by a disk of radius $\theta_{95}^{ext} = 0.45$ deg. Errors are shown by the bars (statistical) and the grey band (systematic). The lines represent the pionic gamma-ray spectra produced by the Galactic CR proton at IC 443 scaled up by a factor of 100 (dashed) and by the locally accelerated proton population with the best-fit broken power-law spectrum described in the text (dot-dash).

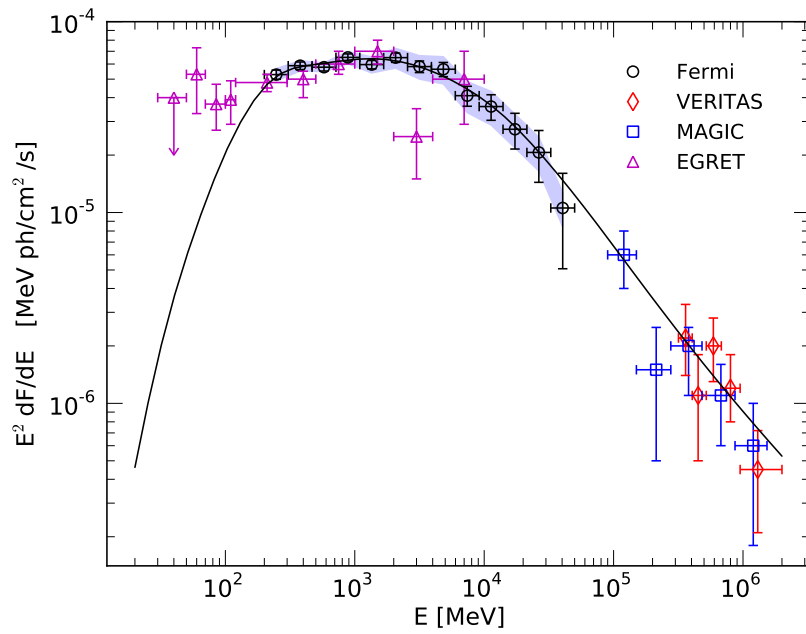


Fig. 4.— Broadband spectral energy density of the 4 sources: *EGRET* (purple triangles), *MAGIC* (blue squares), *VERITAS* (red diamonds) and *Fermi* (black circles). The solid line is the same as the dot-dash line in Fig.3. The systematic and statistical errors of the Fermi data points are also the same as in Fig. 3.

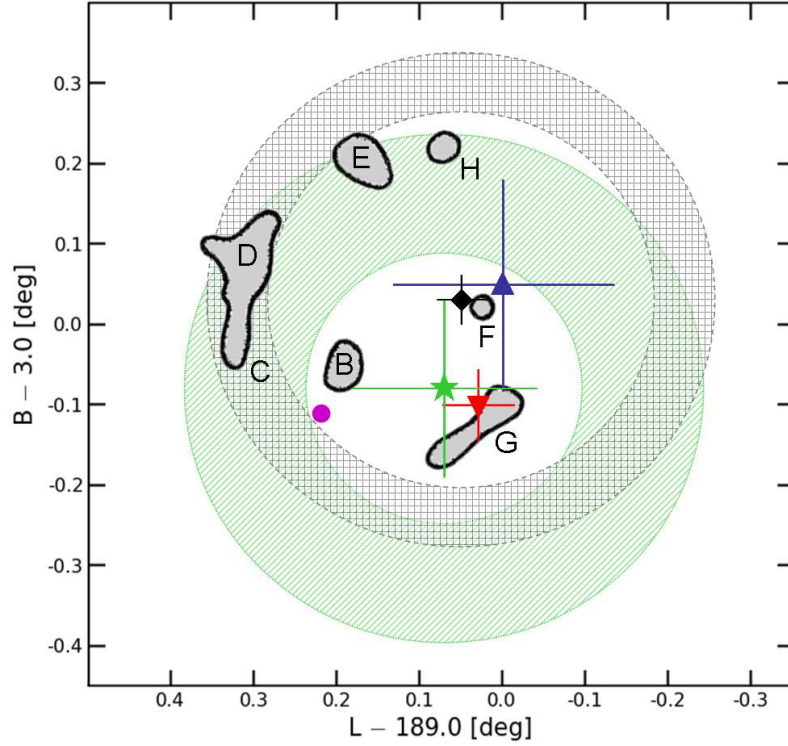


Fig. 5.— Locations and extensions of the 4 gamma-ray sources: *EGRET* centroid (\triangle); *MAGIC* centroid (∇); *VERITAS* centroid (star) and *Fermi* LAT centroid (\diamond). The respective localization errors as tabulated in Table 5 are shown as crosses. Best-fit spatial extensions of the *Fermi* (cross-hatched band) and *VERITAS* (striped green band) sources are drawn as rings with radii of θ_{68}^{ext} and widths of $\pm 1\sigma$ error. The PWN location is shown as a dot. Contours are the locations and shapes of the local shocked molecular clouds taken from Huang et al. (1986).

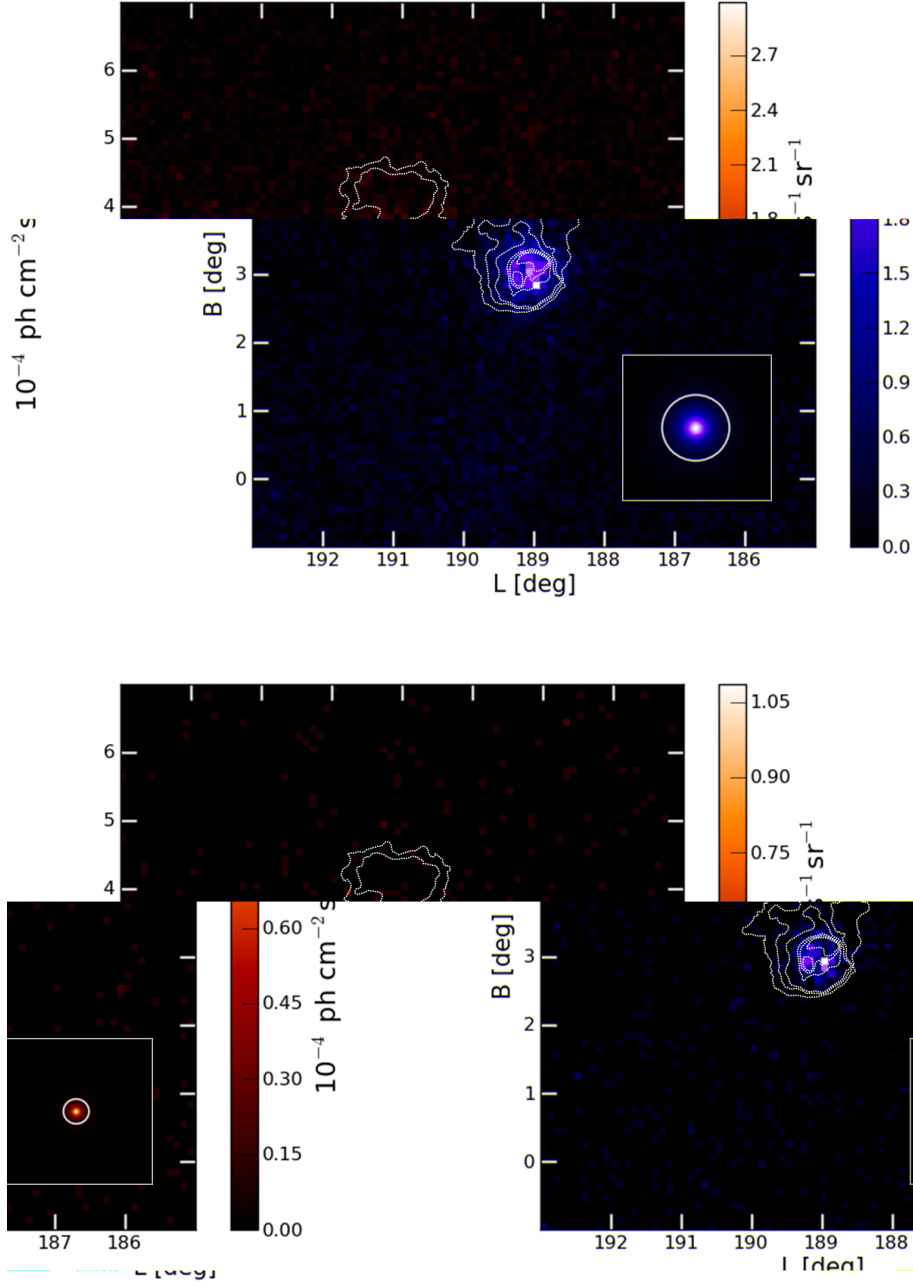


Fig. 1.— Intensity map of the IC 443 region in the 1 – 5 GeV (left) and 5 – 50 GeV (right) bands. Units of intensity are $10^{-4} \text{ cm}^{-2} \text{ s}^{-1} \text{ sr}^{-1}$ for the color scale. The overlay is the 2.7 GHz radio continuum contours taken from Furst et al. (1990). The insets are the spectrum-weighted LAT PSF for each energy band, with the white circles showing the corresponding θ_{68}^{psf} .